ACS Partner Journal

CHEMICAL & BIOMEDICAL IMAGING

Open Access

This article is licensed under CC-BY-NC-ND 4.0

pubs.acs.org/ChemBioImaging

Article

Duplex Unwinding Mechanism of Coronavirus MERS-CoV nsp13 Helicase

Wei Hao,[#] Xiao Hu,[#] Qixin Chen, Bo Qin, Zhiqi Tian, Ziheng Li, Pengjiao Hou, Rong Zhao, Hamza Balci,* Sheng Cui,* and Jiajie Diao*

Cite This: *Chem. Biomed. Imaging* 2025, 3, 111−122

Read Online

ACCESS | Metrics & More | Article Recommendations | Supporting Information

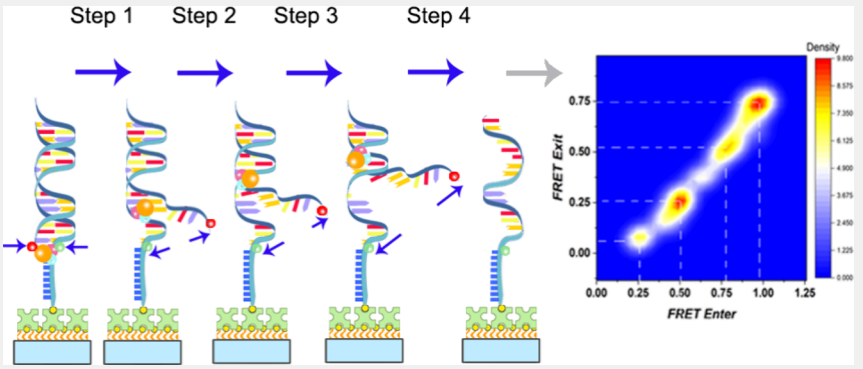

ABSTRACT: The COVID-19 pandemic has underscored the importance of in-depth research into the proteins encoded by coronaviruses (CoV), particularly the highly conserved nonstructural CoV proteins (nsp). Among these, the nsp13 helicase of severe pathogenic MERS-CoV, SARS-CoV-2, and SARS-CoV is one of the most preserved CoV nsp. Utilizing single-molecule FRET, we discovered that MERS-CoV nsp13 unwinds DNA in distinct steps of about 9 bp when ATP is employed. If a different nucleotide is introduced, these steps diminish to 3−4 bp. Dwell-time analysis revealed 3−4 concealed steps within each unwinding process, which suggests the hydrolysis of 3−4 dTTP. Combining our observations with previous studies, we propose an unwinding model of CoV nsp13 helicase. This model suggests that the elongated and adaptable 1B-stalk of nsp13 may enable the 1B remnants to engage with the unwound single-stranded DNA, even as the helicase core domain has advanced over 3−4 bp, thereby inducing accumulated strain on the nsp13-DNA complex. Our findings provide a foundational framework for determining the unwinding mechanism of this unique helicase family.

KEYWORDS: *MERS-CoV, SARS-CoV-2, nsp13 helicase, smFRET, unwinding mechanism*

INTRODUCTION

Coronaviruses (CoVs) have proven to be significant threats to public health and the global economy, as underscored by the COVID-19 pandemic. This pandemic represents the third major CoV outbreak in the past two decades, with its widespread impacts eclipsing those of the severe acute respiratory syndrome (SARS) outbreak in 2002 and 2003[1,2] and the Middle East respiratory syndrome (MERS) outbreak in 2012.[3]

SARS-CoV-2,[4] the pathogen responsible for COVID-19, is recognized as the seventh human CoV,[5] exhibiting approximately 80% nucleotide sequence similarity with SARS-CoV. Greater sequence variation is evident in the structural (i.e., envelope E, membrane M, nucleocapsid N, and spike S) and accessory proteins (i.e., ORF3a or 3b, 6, 7a or 7b, 8, and 10) of SARS-CoV-2 compared to SARS-CoV, yet their nonstructural proteins remain highly conserved.[6] Intriguingly, the key components of the viral RNA replication transcription complex's nonstructural proteins (nsp)—specifically, nsp13 (helicase) and nsp12 (RNA-dependent RNA polymerase)—show more than 98% identical sequences. Remarkably, the nsp13 helicase, encoded by the three highly pathogenic CoVs—SARS-CoV, MERS-CoV, and SARS-CoV-2—shares 84% to 99% sequence similarity, highlighting its potential as a broad-spectrum antiviral target which has been further highlighted with identification of potential druggable pockets in the crystal structure of SARS-CoV-2 nsp13 helicase.[7] The nsp13, a member of the SF1B helicase family, unwinds RNA and DNA duplexes with a 5′-to-3′ directionality and possesses

Received: October 4, 2024
Revised: December 6, 2024
Accepted: December 9, 2024
Published: December 19, 2024

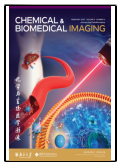

ACS Publications

© 2024 The Authors. Co-published by Nanjing University and American Chemical Society

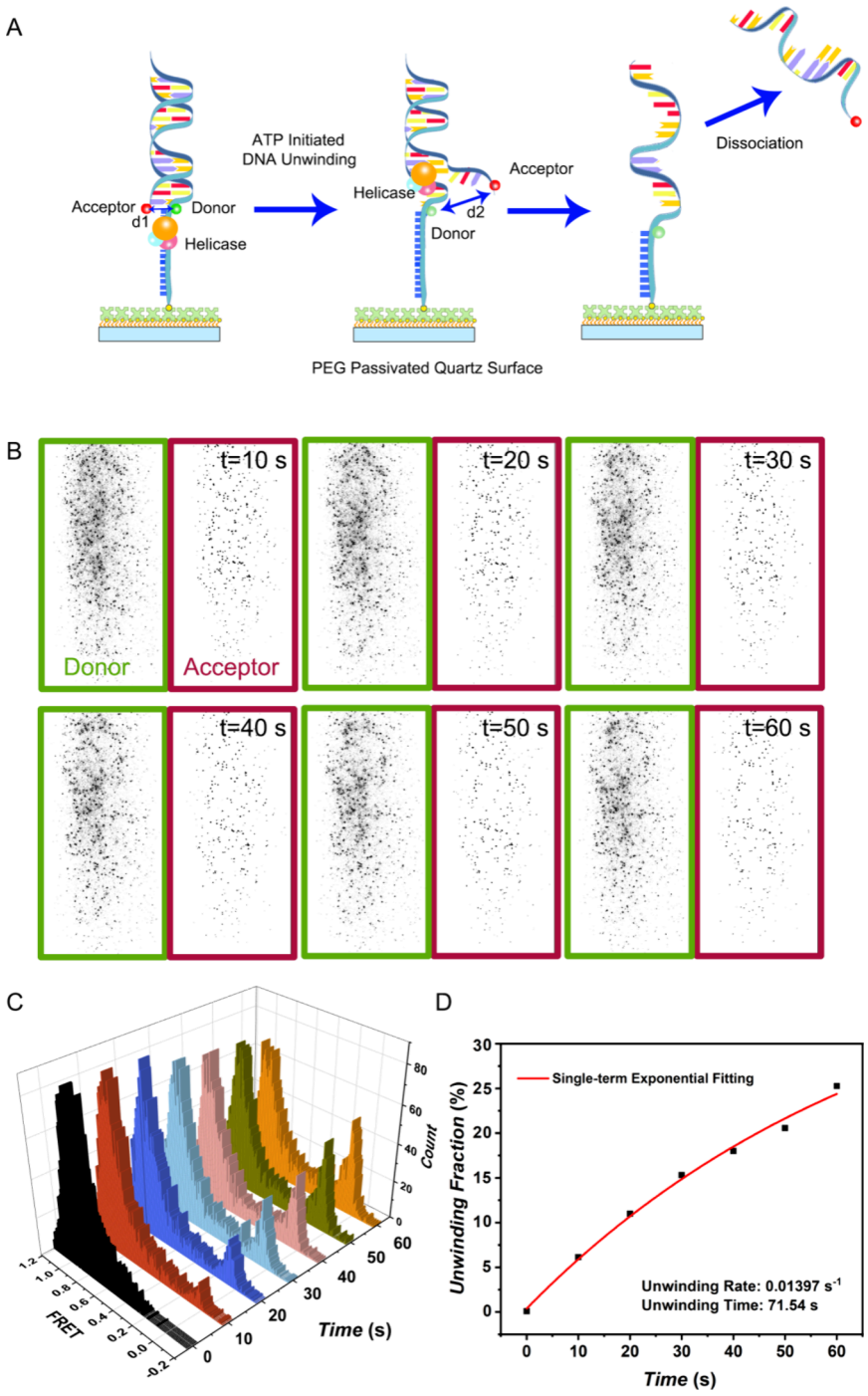

Figure 1. MERS-CoV nsp13 helicase unwound a significant fraction of double-stranded DNA (dsDNA) within 1 min with ATP. (A) Schematic illustration of DNA unwinding by MERS-CoV nsp13 helicase using ATP. (B) Fluorescent images of DNA in the corresponding donor (Cy3) and acceptor (Cy5) channels 1 min after the addition of ATP. (C) Histograms showing FRET efficiency as a function of time representing populations of unwound DNA (low FRET) and intact DNA (high FRET). All histograms were created using DNA molecules possessing both acceptor and donor fluorophores. (D) Time-dependent representation of unwound DNA (fraction of low FRET population) derived from the histograms in (C); an overall exponential fit to the curve demonstrates an unwinding rate, R, of 0.014 s^{-1} and an unwinding time of 71.54 s. The unwinding experiment was performed with 20 nM nsp13, 3 mM $MgCl_2$, and 400 μM ATP.

both nucleoside triphosphate (NTP) and deoxynucleotide triphosphates (dNTP) hydrolyzing activity, as well as hosting 5′-triphosphatase activity.[8,9] Our previous studies elucidated the crystalline structure of MERS-CoV nsp13 (PDB ID: 5WWP), demonstrating that while nsp13 broadly aligns with the domain organization of nidovirus helicases, the individual domains (CH, RecA1−1B, and RecA2) of nsp13 are analogous to the organization of cellular Upf1-like helicases.[10,11]

Investigations into the mechanisms of CoV nsp13 helicases have predominantly employed ensemble methods.[12] The SARS-CoV nsp13 exhibits a preference for substrates characterized by extensive 5′ single-stranded DNA (ssDNA) tails or gaps for duplex unwinding. Enhanced processivity of

https://doi.org/10.1021/cbmi.4c00077
Chem. Biomed. Imaging 2025, 3, 111−122

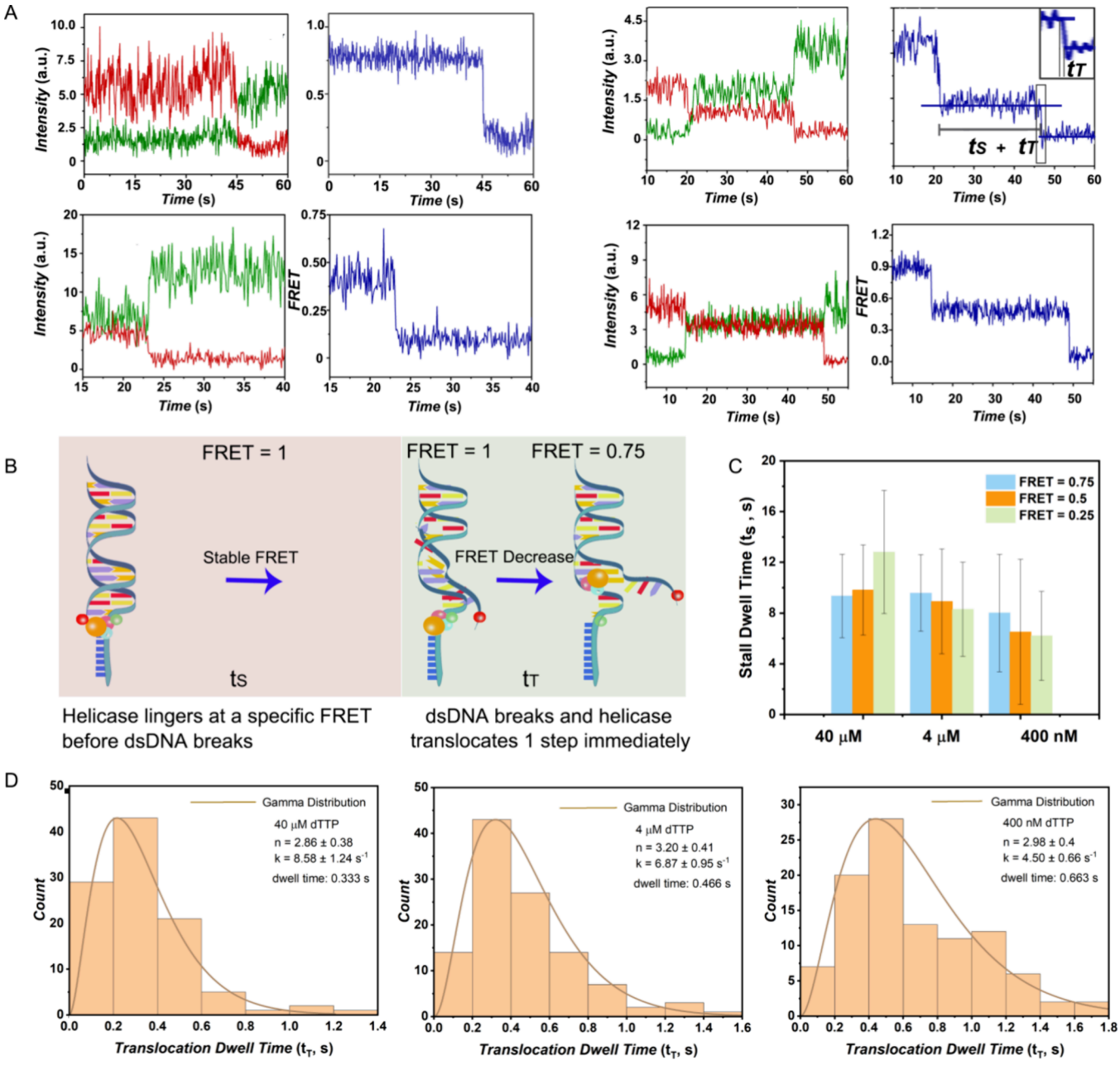

Figure 2. MERS-CoV nsp13 helicase unwound dsDNA in single or multiple steps and stalled at specific unwinding stages (FRET states) before commencing the next. (A) Representative fluorescence intensity and corresponding FRET efficiency time traces of unwinding processes. (B) Scheme of the stall-and-translocate unwinding process by MERS-CoV nsp13. (C) Stall dwell time (t_S) of each state at varying concentrations of chemical energy; 220 molecules undergoing a multistep unwinding process were utilized for dwell time calculation. (D) Gamma distribution fit of collected translocation dwell times (t_T); the t_T at 40 μM, 4 μM, and 400 nM dTTP was calculated from 102, 111, and 101 molecules, respectively. The chi-square values for Figure 2D are 2.669, 1.335, and 0.226 respectively. The observed data were not significantly different from the expected gamma distribution at $p < 0.05$. The Unwinding experiments were performed with 20 nM nsp13, 3 mM $MgCl_2$, and varied concentrations of dTTP (indicated in the figure).

DNA unwinding is associated with the loading of multiple nsp13 molecules onto the 5′ ssDNA regions.[13] A translocation mechanism for nsp13 has been postulated following the results of a hydrogen−deuterium exchange assay,[14] depicting the grasp and release of ssDNA relay between the RecA1−1B and RecA2 domains of nsp13. This mechanism correlates with the three transition states of adenosine triphosphate (ATP) hydrolysis and closely mirrors the paradigmatic mechanism of the SF1B helicase RecD2.[15] An intriguing aspect of the unwinding reaction catalyzed by nsp13 is the presence of lags, which become more pronounced as the DNA duplex length increases. Sarafianos et al. employed a rapid chemical quench flow method to detect intermediates during dsDNA unwinding by SARS-CoV nsp13 and calculated an average kinetic step size of 9.3 bp per step.[16] However, the mechanism underpinning the lagged unwinding remains unclear.

Given the available structural and biochemical profiles of MERS-CoV and SARS-CoV nsp13, coupled with the minor conservative substitution in SARS-CoV-2 nsp13 (I570 V) relative to SARS-CoV nsp13, we investigated the kinetic

https://doi.org/10.1021/cbmi.4c00077
Chem. Biomed. Imaging 2025, 3, 111−122

mechanism enabling two nsp13 helicases to unwind DNA. Our findings elucidate this distinctive helicase's mechanism and may aid in the development of antiviral agents to address COVID-19, its potential resurgence, and future similar viral disease outbreaks.

RESULTS AND DISCUSSION

MERS-CoV Helicase Rapidly Unwound DNA with ATP

In our previous biochemical characterization, the MERS-CoV nsp13 mechanism of unwinding an 18-bp DNA duplex, which harbors a 5′ overhang, was shown to hinge on NTP hydrolysis. Similarly, the SARS-CoV nsp13 demonstrated the ability to unravel a 15-bp partial DNA duplex with a congruent 5′ overhang.[17] To elucidate this unwinding process, we engineered single-molecule fluorescence resonance energy transfer (smFRET) experiments (Figure 1A). Utilizing the biotin-NeutrAvidin interaction, we anchored partial double-stranded DNAs (dsDNAs) with 5′ ssDNA tails on the imaging surface. This was done with the aid of biotin at the 5′ termini of the ssDNA overhangs. The partial dsDNA was comprised of an 18-base top strand, labeled at the 3′ end with Cy5 as the acceptor, and a 39-base bottom strand, marked at the ssDNA-dsDNA junction with Cy3 as the donor. The conjoining of the top and bottom strands produced a partial duplex with a 21 nt ssDNA overhang. We hypothesized that the processivity of CoV nsp13-catalyzed unwinding could be augmented if several enzymes concurrently bind to the 5′ ssDNA overhangs of the substrate. Hence, we explored the binding dynamics between MERS-CoV nsp13 and this partial DNA duplex via an electrophoretic mobility shift assay (EMSA). After incubating the enzyme with the partial DNA duplex in the buffer used for smFRET, the resultant mixtures were differentiated by native-PAGE (Figure S1). In our EMSA experiment, a single band was observed, indicative of the DNA-nsp13 complex's size with a 1:1 stoichiometry. The band's intensity amplified with increasing protein concentration, and no higher molecular weight DNA-nsp13 species were observed at the highest protein concentration. This outcome verifies that under smFRET conditions, a single nsp13 molecule is bound to one DNA substrate.

Upon preincubation of 20 nM full-length MERS-CoV nsp13 protein with the DNA substrate, the initiation of the reaction was triggered by injecting 400 μM ATP, enabling real-time documentation of the unwinding process. The resulting FRET efficiencies encapsulated different unwinding states. In the absence of ATP, nsp13 was found to bind to the ssDNA portion of the partial duplex, thereby facilitating sustained proximity between the donor and acceptor and leading to high FRET values. With the subsequent introduction of ATP, nsp13 commenced translocation on the bottom strand toward the 3′ end, concurrently unzipping the DNA duplex. As the donor and acceptor separated, a gradual decrease in the FRET values was observed. The unwinding process was imaged using total internal reflection fluorescence (TIRF) microscopy, with representative real-time images of donor and acceptor channels after 1 min of ATP injection depicted in Figure 1B. Accompanying acceptor/donor counts from Figure 1B are presented in Table S1.

We evaluated the FRET efficiencies corresponding to the immobilized dsDNAs at varying time points after ATP injection (Figure 1C). Resulting histograms indicated a high FRET peak preceding a low one, representative of the initial dsDNAs and unwound DNAs, respectively. Before the introduction of ATP (at time 0), the majority of the dsDNAs demonstrated high FRET efficiencies with negligible low FRET peaks. Following ATP injection, high FRET peaks showed a temporal decrease, with a concurrent increase in the low FRET peak. Subsequently, we plotted the unwound population over time (Figure 1D). During the initial phase of the reaction, MERS-CoV nsp13 demonstrated rapid unwinding, which slowed over time, likely attributed to the depletion of the DNA duplex in the system. Roughly 41% of the total dsDNA population was unwound after 1 min. Assuming a binary state for the unwinding process—intact or unwound—the characteristic unwinding rate (R) and time (T) could be determined by fitting the evolution of the unwound population with a single exponential function, yielding R = 0.01397 s^{-1} and T = 71.54 s for the selected experimental condition. Control experiments were also conducted under similar experimental conditions, excluding one of the necessary unwinding components (ATP/Mg^{2+}/nsp13) to substantiate that the decrease in FRET efficiency was indeed caused by the unwinding process (Figure S2).

MERS-CoV nsp13 Exhibited Single and Multiple Steps in Unwinding Influenced by NTP Types

In our experiments, we observed that the MERS-CoV nsp13 helicase unwound the DNA duplex in both single-step and multistep fashion. Figure 2A shows representative traces of different unwinding events. The traces on the left exhibit one FRET reduction, indicative of a one-step unwinding process. Conversely, the traces on the right depict two FRET transitions, suggesting a two-step unwinding process with a step size of approximately 9 bp (a shorter step size is feasible, as the last few intact base pairs of dsDNA may not be stable enough and spontaneously break due to thermal energy, simultaneously with the last step of helicase). The observed stable intermediary FRET values imply that MERS-CoV nsp13 momentarily halts DNA unwinding under specific conditions. This corroborates previous ensemble research on SARS-CoV nsp13-mediated unwinding reactions,[16] where Sarafianos et al. reported intermediates in the DNA unwinding by SARS-CoV nsp13. Through a presteady-state kinetic assay, they approximated the unwinding step to be 9.3 bp, which is consistent with the step size we measured for MERS-CoV nsp13.

In order to elucidate the multistep unwinding process, we modulated the unwinding rate by introducing different chemical energy sources. Helicases demonstrate various NTP preferences; for instance, hepatitis C virus (HCV) NS3 hydrolyzes all eight canonical NTPs with a preference sequence of (d) ATP > (d) CTP > UTP or dTTP > (d) GTP.[18] Therefore, we employed various NTPs (i.e., ATP, GTP, CTP, and dTTP) to fuel the unwinding reactions and successfully achieved slower unwinding rates using alternative NTPs as energy sources (particularly dTTP) or at reduced concentrations (i.e., 4 mM to 400 nM). As anticipated, the decrease in unwinding rate increased the occurrence of the multistep unwinding events (Figure S3).

The analyses of the trace curves demonstrated that MERS-CoV nsp13 helicase unwound the dsDNA in a sequential manner. In particular, MERS-CoV nsp13 demonstrated a pattern of stalling at a given unwinding step, referred to as a FRET state, prior to progressing to the subsequent stage (Figure 2B). This stalling process is expressed as "dwell time," or the difference between FRET exit and enter time. The dwell

https://doi.org/10.1021/cbmi.4c00077
Chem. Biomed. Imaging 2025, 3, 111−122

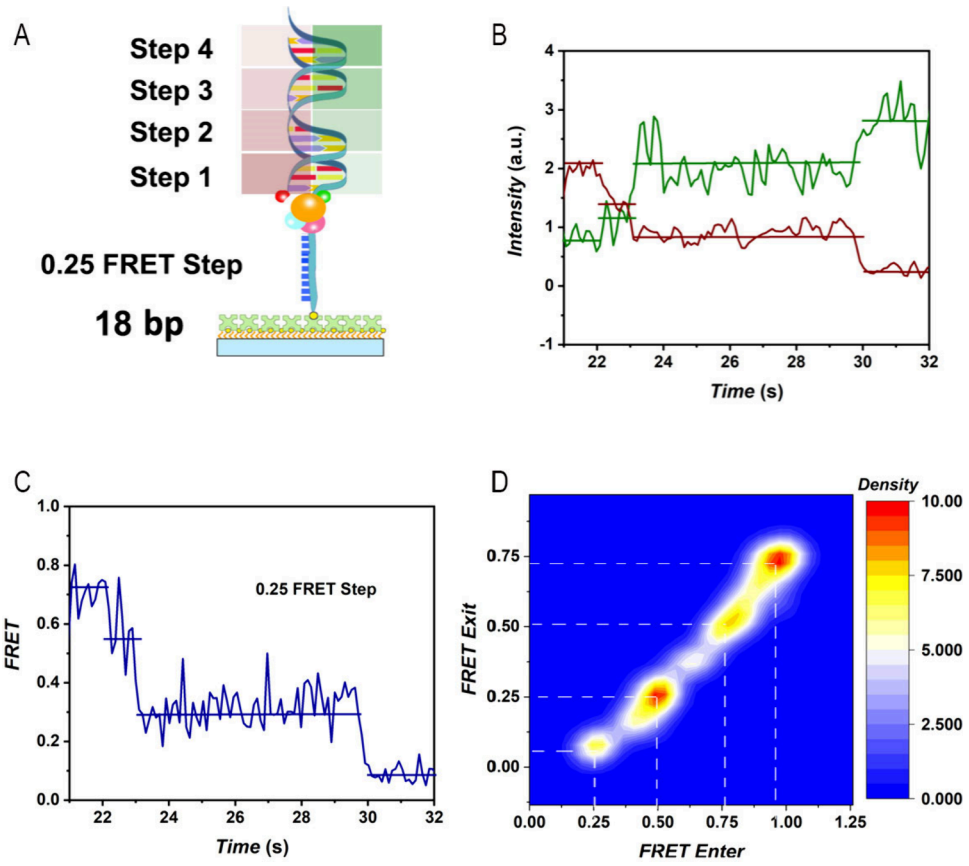

Figure 3. MERS-CoV nsp13 helicase unwound 18-dsDNA in 4 discrete steps, fueled by dTTP. (A) Schematic illustration of DNA unwinding by MERS-CoV nsp13 helicase using dTTP. Representative fluorescence intensity (B) and corresponding FRET efficiency time traces (C) of unwinding processes. (D) FRET values obtained from 140 multistep traces were combined to create the transition density plot for the 18-bp dsDNA. Unwinding experiments were performed with 20 nM nsp13, 3 mM $MgCl_2$, and 400 μM of dTTP.

time encompasses two components: stall dwell time (t_S), or the duration in which the helicase remains static at a specific location (FRET state) prior to the disruption of the dsDNA, and translocation time (t_T). The t_S of the helicase is influenced more by factors such as DNA sequence and fork tension for passive helicases such as nsp13, rather than by energy concentration. The t_S at each FRET state was determined from the multistep unwinding process observed in 216 molecules. The findings (Figure 2C), suggest that MERS-CoV nsp13 displayed a stall time of approximately 7 ± 5 s at every FRET state before proceeding to the subsequent step for our DNA construct. Dwell time histograms are shown in Figure S4.

The translocation time (t_T) represents the duration spent by the helicases in each dTTP-powered translocation event. Figure 2D presents a t_T histogram of individual translocation events at various dTTP concentrations. As the t_T histogram did not exhibit a single-exponential decay, this suggests the presence of hidden irreversible Poisson steps within the individual events observed. Gamma distribution $t^{n-1}\ exp(-kt)$ was used to fit the t_T histogram, and the calculated shape parameters n were 2.86 ± 0.38, 3.20 ± 0.41, and 2.98 ± 0.40; and rate parameters k were 8.58 ± 1.24 s^{-1}, 6.87 ± 0.95 s^{-1}, and 4.50 ± 0.66 s^{-1} for 40 μM, 4 μM, and 400 nM dTTP, respectively. These shape parameters, n, represent the hidden irreversible Poissonian steps in the hydrolysis of approximately three NTPs, whereas the rate parameters, k, correspond to the hydrolysis rate for a single NTP. Average t_T values of 0.333 0.466, and 0.663 s were respectively obtained for each translocation event using dTTP concentrations of 40 μM, 4 μM, and 400 nM. The size of each translocation event is estimated to be 3−4 bp since an 18-bp duplex is unwound in four steps. The uncertainty in this estimate primarily arises due to the inability to rule out the last few remaining base pairs spontaneously breaking due to thermal energy, rather than helicase activity. Based on these observations, MERS-CoV helicase undergoes a sudden 3−4 bp movement following three consecutive dTTP hydrolysis events.

MERS-CoV nsp13 Unwound the 18 bp dsDNA in 4 Discrete Steps

The transition density plot (Figure 3), summarizes the MERS-CoV nsp13-facilitated unwinding of an 18-bp dsDNA, compiled from 140 transition instances with associated FRET alterations of approximately 0.25. Emergent peaks with enter/exit FRET values were noted at roughly 0.97/0.75, 0.76/0.51, 0.50/0.26, and 0.25/0.07. This plot confirmed that the 0.25 FRET length was the smallest recorded unwinding step and that the 18-bp unwinding process, with dTTP, exhibited four unique steps.

A calibration was performed between the FRET efficiency and the length of unwound duplex DNA. A fully complementary duplex DNA substrate yielded a FRET efficiency around 1, a 9 nt opened duplex DNA achieved a FRET efficiency near 0.5, and a fully opened substrate demonstrated 0 FRET efficiency (Figure S5). The unwinding sequence with a 24-bp dsDNA was further scrutinized, with findings

https://doi.org/10.1021/cbmi.4c00077
Chem. Biomed. Imaging 2025, 3, 111−122

documented in Figure S6. It was observed that the trace curves and transition density plot showcased four discrete steps (1−18 bp) on the 24-bp dsDNA. The latter steps (19−24 bp) could not be delineated due to the diminished sensitivity of FRET in the low FRET value range. A recent study on SARS-CoV-2 nsp13 helicase showed that this helicase unwound 16−30 bp long double stranded RNA with similar efficiency,[19] suggesting the helicase is processive in this length range. Our results suggest that MERS-CoV nsp13 helicase remains processive in dsDNA of similar length.

Single-Point Mutations Affected the Unwinding Rate of MERS-CoV nsp13

Further elucidation of the unwinding mechanism prompted a mutagenesis study of 13 invariant residues in SARS-CoV and SARS-CoV-2 nsp13, strategically selected from the nucleic acid binding groove of MERS-CoV nsp13 (Figure 4). We predicted that the selected residues would contact ssDNA based on the modeled structures of CoV nsp13-DNA. This modeling was achieved by superimposing the unliganded structures of MERS-CoV nsp13 (PDB id: 5WWP)[10] and SARS-CoV-2 (PDB id: 6ZSL) onto the EAV nsp10-ssDNA complex (PDB id: 4N0O). The series of mutations incorporated were S310D, H311D, T359D, N361D, A362D, and P408D in the RecA1 domain; R178D in the 1B domain; and Y515D, N516D, T532D, D534A, S535D, and R560D in the RecA2 domain (Figure 4A and B). The unique characteristics of the selected residues were observed to be 2-fold. First, all of the selected residues exhibited structural counterparts in EVA nsp10, previously verified to be involved in DNA binding through X-ray crystallography, as delineated in Table 1. Second, the residues were situated on conserved DNA-binding motifs; S310 and H311 from motif Ia and P408 from motif III coalesced to form a conserved pocket analogous to the motif Ia pocket in RecD2's 1A domain, which has the potential to accommodate a DNA base. Residues T359, N361, and A362, located in the loop between β18 and β19, were positioned at the ssDNA binding channel's entrance, proximate to the 3′ end of the modeled ssDNA. This location was commensurate with the pin device in RecD2 helicase, though it was notably shorter in nsp13 and lacked a rigid β-hairpin structure. The segment from Y515 to N516, found in the loop between β23 and α14, was situated at the 5′ end terminus of the modeled ssDNA. T532, D534, and S535 from motif V constructed a short helix beneath the phosphodiester backbone of the modeled ssDNA, with R560 from motif VI potentially interacting with the base and sugar moiety of the ssDNA. R178 from the 1B domain established interaction with the modeled ssDNA, thus potentially causing a halt in unwinding by anchoring ssDNA to the 1B domain. Conserved threonine pairs—T359 and T532, one threonine on each RecA-like domain—are a common feature in MERS-CoV, SARS-CoV, and SARS-CoV-2 nsp13 helicases, as well as in numerous structurally characterized helicases, including SF1A helicases (Rep, UvrD, PcrA, and others), SF1B helicase (RecD2, and others), and SF2 helicase (HCV NS3, and others). The threonine pair functions as a reference for understanding the translocation mechanism, whereupon ATP binding to a helicase places the threonine residues 2 bp apart, and their absence results in a 3 bp separation.[20] This observation corroborates the prevailing 1 bp translocation and 1-ATP hydrolysis theory. In the nsp13-ssDNA model representing an ATP-deprived condition, the threonine pair's 3 bp separation further supports this theory.

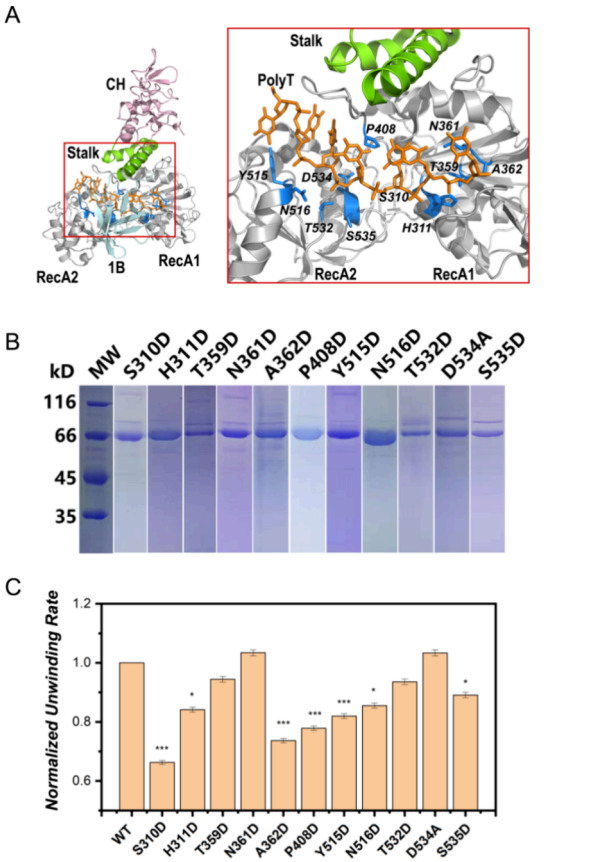

Figure 4. Single-point mutations in the RecA1 and RecA2 domains affected the unwinding activity of the MERS-CoV nsp13 helicase. (A) Structure-guided mutagenesis. Left: ribbon model of MERS-CoV nsp13 with a modeled poly(dT) ssDNA strand. The individual domains of nsp13 are color-coded: CH domain in pink, stalk domain in green, 1B domain in cyan, and helicase core (RecA1 and RecA2) in gray. The poly(dT) in the orange stick model was modeled by superimposing MERS-CoV nsp13 with EAV nsp10-ssDNA complex (PDB ID: 4N0O). To the right, a magnified view of the boxed area from the left depicts the putative RNA binding groove of MERS-CoV nsp13. Residues predicted to interact with DNA are represented in the blue stick model and are italicized. Substitutions were introduced into each residue, which yielded 11 helicase mutants: S310D, H311D, T359D, N361D, A362D, P408D, Y515D, N516D, T532D, D534A, and S535D. The unwinding activities of these mutants were evaluated with smFRET in (C). (B) SDS-PAGE gel image of 11 MERS-CoV nsp13 mutants. (C) Normalized unwinding rates of the WT and the different single-point mutants. Student's *t*-test was used to determine the statistical significance between the WT and the mutants. $*p < 0.05$, $**p < 0.01$, $***p < 0.005$. The unwinding experiment was performed with 20 nM nsp13, 3 mM $MgCl_2$, and 400 μM of ATP.

Consequently, the structural determination of nsp13 complexed with nucleic acids, both with and without the presence of NTP or its analogues, could provide critical validation of this theory.

Utilizing smFRET, we quantified the unwinding rate of various mutant forms in comparison to that of the wild-type (WT). All mutants, except for R178D and R560D due to their insolubility, were evaluated. The unwinding functionality of most mutants demonstrated detrimental effects (Figure 4C), as shown with the unwinding data given in Table S2 and Figure S7. Unwinding rates of S310D, A362D, P408D, and Y515D significantly declined in relation to WT nsp13 ($p < 0.005$), while the rates for H311D, N516D, and S535D were also

https://doi.org/10.1021/cbmi.4c00077
Chem. Biomed. Imaging 2025, 3, 111−122

Table 1. Residues Predicted to Contact DNA[a]

	MERS-CoVnsp13	SARS-CoVnsp13	SARS-CoV-2 nsp13	EAV nsp10 (4N0O)
1B	*R178*	R178	R178	**R102**
RecA1	*S310*	S310	S310	**T185**
	H311	H311	H311	**H186**
	T359	T359	T359	**L227**
	N361	N361	N361	**Q229**
	A362	A362	A362	**V230**
	P408	P408	P408	**V271**
RecA2	*Y515*	Y515	Y515	**Y338**
	N516	N516	N516	**H339**
	T532	T532	T532	**T348**
	D534	D534	D534	**D350**
	S535	S535	S535	**S351**
	R560	R560	R560	**R374**

[a]Note: Bolded residues indicate confirmed nucleic acid contacts in EAV nsp10, as supported by experimental data (PDB ID: 4N0O). All other residues are predictions, inferred through structural comparison with the EAV nsp10-DNA complex.

notably diminished ($p < 0.01$). The unwinding rates of T359D, N361D, T532D, and D534A, however, did not exhibit significant change. These functional declines, arising from residue substitutions, suggest their critical role in unwinding. Residue P408, for example, comprises one side of a pocket nestled between motifs Ia and III on the RecA1 domain. This "motif Ia pocket" is recognized for its crucial role in DNA translocation, as demonstrated not only in SF1B helicase RecD2,[15] but also in SF1A helicase PcrA.[21,22] During ssDNA translocation, a DNA base occupies RecD2's motif Ia pocket, functioning as a physical barrier to grasp DNA as the 2A and 2B domains glide by. Given that MERS-CoV nsp13 employs an analogous mechanism, the P408D mutation may disrupt the hydrophobic interaction between the DNA base and motif Ia pocket, thereby impairing DNA translocation. Located on a loop between β18 and β19 at the nucleic acid binding channel entrance, residue A362 is posited to bind the ssDNA-dsDNA junction. Upon RecD2 structure overlap, the corresponding region of the β18-to-β19 loop in RecD2 functions as a "pin domain," effectively prying open the DNA-RNA duplex. The substitution of A362 with an aspartate, therefore, might obstruct duplex separation rather than inhibit DNA translocation.

Difference in Activity between MERS-CoV and SARS-CoV-2 Helicases

SARS-CoV-2 nsp13 and MERS nsp13 display substantial structural similarity, exhibiting a Dali Z-score of 45.4 and an rmsd of 2.3 Å across 572 aligned Cα atoms, alongside an 84% amino acid sequence similarity and 71% sequence identity. It remains an open question whether these sequence variations impact their distinct enzymatic activities. Utilizing a malachite-green-based NTPase assay (Figure 5), the NTPase turnover rate of MERS-CoV nsp13 and SARS-CoV-2 nsp13 was analyzed. The assays were conducted with a fixed enzyme concentration (50 nM) and nucleotide triphosphate substrate concentration (125 μM), with both nsp13 helicases devoid of affinity tags. A Walker B mutant E375Q of SARS-CoV-2, generated via site-directed mutagenesis, served as a catalytically inactive control (Figure S8B). Both MERS-CoV nsp13 and SARS-CoV-2 nsp13 demonstrated a stronger affinity for ATP over those of CTP and dNTP during hydrolysis. Intriguingly,

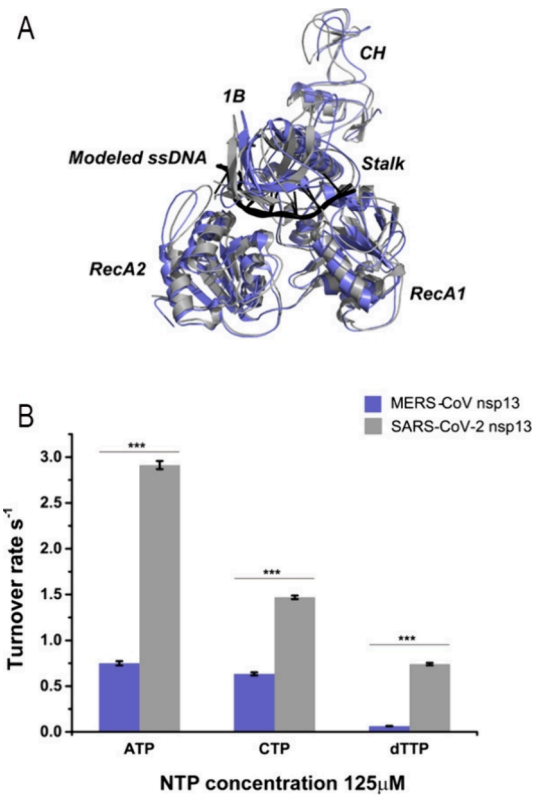

Figure 5. Comparison of nucleotide hydrolysis activity among different nsp13 helicases. (A) Modeled structures of superimposed MERS-CoV nsp13-DNA (blue) and SARS-CoV-2 nsp13-DNA (gray). (B) Turnover rates (per second) of different nucleotide substrates ATP, CTP, and dTTP by MERS-CoV nsp13 (blue) and SARS-CoV-2 nsp13 (gray). For each turnover rate assessment, a minimum of six independent measurements were performed to calculate the velocity of NTP hydrolysis. ***$p < 0.0001$.

MERS-CoV nsp13 showed a significantly reduced turnover rate compared to SARS-CoV-2 nsp13 in hydrolyzing different nucleotide triphosphates, suggesting enhanced NTP hydrolysis capability of SARS-CoV-2 nsp13. For dTTP, the least preferred substrate, SARS-CoV-2 nsp13 showcased a hydrolysis activity that was 11.5 times higher than MERS-CoV nsp13. In the cases of ATP and CTP, the turnover rates of SARS-CoV-2 nsp13 were greater by 3.9- and 2.3-fold, respectively. Whether the difference in NTP hydrolysis contributes to the unwinding activities of CoV nsp13 helicases, however, requires an in-depth single molecule level analysis.

CONCLUSION

Available biochemical and structural evidence suggests that the CoV nsp13 translocation model aligns with the canonical 5′-to-3′ translocation mechanism characteristic of SF1B helicases.[15] Prior to our study, the duplex-unwinding mechanism of nsp13 was elusive. Certain helicases such as RecD2, RecG, and Hel308a[15,23,24] deploy a firm pin or wedge at the ssDNA-dsDNA intersection to pry open base pairs; this device, however, seems absent in CoV nsp13, or an analogous component in nsp13 has yet to be identified. Rao et al. reported a β19-to-β20 loop in SARS-CoV nsp13, comparable to a β17-to-β18 loop in MERS-CoV nsp13, hosting a selection of conserved, positively charged residues, for instance, arginine and lysine. They established that this region, despite being instrumental to nsp13-catalyzed unwinding activity, only binds

https://doi.org/10.1021/cbmi.4c00077
Chem. Biomed. Imaging 2025, 3, 111−122

to the partial DNA duplex, not to ssDNA exclusively. As such, further exploration is needed to understand this region's role in the unwinding process, particularly in defining the structures of nsp13-nucleic acid complexes. Previous research indicated that helicases can actively or passively unwind double-stranded nucleic acids. Helicases incorporating a pin device are predisposed to direct nucleic acid base-pair destabilization, leading to active duplex opening. Conversely, helicases without a comparable device are expected to unwind the double-stranded nucleic acid indirectly or passively, potentially through binding to the transiently opened single-strand region of the duplex.[25,26] In line with this theory, both SARS-CoV-2 nsp13-catalyzed RNA duplex unwinding, as reported by Mickolajczyk et al.,[19] and the MERS-CoV nsp13-catalyzed DNA duplex unwinding, as presented in this paper, appear to employ a passive mechanism.

Our smFRET experiment clearly demonstrated that MERS-CoV nsp13 catalyzes the unwinding of dsDNA (specifically, an 18-bp partial duplex) in distinct steps of approximately 9 bp in the presence of ATP. Interestingly, when different NTPs are used, the step size reduces to approximately 3−4 bp, thereby indicating the existence of a lag, i.e., unwinding intermediates. This observation aligns closely with the conclusions of a previous ensemble study,[16] in which researchers, employing a rapid chemical quench flow instrument, determined that SARS-CoV nsp13 unwinds dsDNA in discrete steps of 9.3 bp at a catalytic rate of 30 steps per second. This lag phenomenon in duplex unwinding is suggestive of the spring-loaded unwinding mechanism characteristic of the HCV NS3 helicase (HCV NS3-Hel).[27] In HCV NS3, an aromatic residue (W501) stacks against the 3′ terminus base of DNA, thereby anchoring the DNA to the D3 domain. The two RecA-like D1 and D2 domains of NS3-Hel translocate in a 3′ to 5′ direction along the DNA. Concurrently, the interaction between D3 and the DNA results in a delay in duplex unwinding. When the accumulated tension reaches a critical threshold, a rapid movement of the D3 domain occurs, resulting in a burst of 3-bp unwinding. A patrolling mechanism for HCV NS3-Hel has been postulated;[28] however, our smFRET experiments did not detect any patrolling events (Figure S9), a finding corroborated by another single-molecule force study[19] proposing a processive model for SARS-CoV-2 nsp13. Although we did not observe it, we cannot dismiss the possibility that under certain conditions nsp13 may adopt a more active unwinding mechanism, as implied by previous helicase research.[29] For instance, the DnaB helicase was postulated to function as an active helicase under specific DNA-pulling geometries,[30] and the T7 gp4 showed enhanced activity when bound to its polymerase.[31] Further research is necessary to explore this potential.

We postulate that the 1B domain of CoV nsp13 might function similarly to that of D3 of NS3-Hel, albeit via a different mechanism. Based on the modeled structures of MERS-CoV nsp13 and SARS-CoV-2 nsp13 bound to ssDNA, as illustrated in our previous study,[10] the 1B domain and the RecA1 domain coalesce to encapsulate the 3′ portion of the ssDNA. The motif Ia pocket interfaces with the DNA on one flank, whereas the conserved residues, namely 178R to 179N, of the 1B domain interact with the DNA on the alternate flank. Driven by the energy derived from NTP hydrolysis, the RecA1 and RecA2 domains proceed in a 5′ to 3′ direction, while the 1B domain remains static in relation to the DNA. Unlike the D3 of NS3-Hel, the 1B domain is linked to the body of the helicase core via a relatively extended (approximately 20 Å) stalk domain.[32] This unique flexible architecture enables considerable interdomain rearrangement; hence, the 1B-DNA interaction may withstand a lag of more than 3−4 bp behind the translocating RecA1 and RecA2 domains.

Finally, we propose a model of CoV-nsp13-catalyzed duplex unwinding by combining previous publications and our findings (Figure 6). During the substrate loading process, the

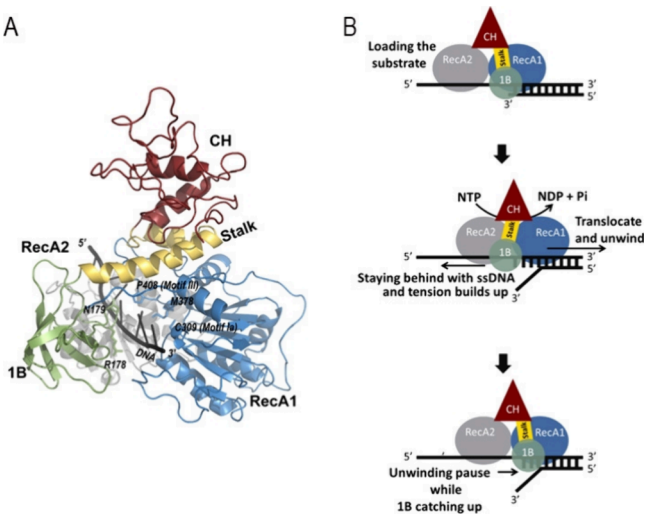

Figure 6. A model of CoV nsp13 unwinding. (A) Modeled structure of MERS-CoV nsp13 complexed with ssDNA. The individual domains are color-coded: CH domain in red, stalk domain in yellow, 1B domain in green, RecA1 domain in blue, and RecA2 domain in gray. DNA is depicted in black. Key residues constituting the conserved domain between motifs Ia and III are displayed in a stick model. Residues from the 1B domain, which interacted with the DNA on the opposite side, are illustrated in another stick model. (B) A model of how CoV nsp13 translocates on DNA and unwinds the duplex in 3−4-bp discrete steps. Briefly, the 1B and RecA1 domains of nsp13 sandwich the ssDNA portion of the partial duplex. Fueled by the energy from NTP hydrolysis, the RecA1 and RecA2 domains translocate forward in a direction from 5′ to 3′, simultaneously unwinding the DNA duplex, while the 1B remains stationary with the unwound ssDNA, thus lagging temporarily, as illustrated in panel B, middle. Because the 1B is distantly connected to the body of the helicase core via the stalk domain, this flexible architecture permits the distance between 1B and RecA1 to be a maximum of 3−4 bp. When the tension reaches a breaking point, the unwinding temporarily pauses. At this moment, 1B loosens its grip on ssDNA and finally resumes its original formation (panel B, bottom).

helicase core RecA1/RecA2 domains bind the 5′ ssDNA overhang at the ss-ds junction of the dsDNA substrate. Concurrently, the 1B domain attaches to the ssDNA on the side contrary to the RecA1 domain. As suggested by the nsp13-DNA model, the 1B domain likely functions to stabilize DNA binding. As NTP infiltrates the active site, RecA2 intensifies its hold on ssDNA; in contrast, RecA1 slackens its grip on DNA, gravitating toward the 3′ end. Employing an as-yet unidentified molecular apparatus (a consequence of the absence of nsp13-DNA structures), reminiscent of the rigid pin or wedge observed in other helicases, the RecA1 domain disjoints DNA base pairs, harnessing the energy from NTP hydrolysis. Subsequently, the RecA1 domain strengthens its bond with ssDNA, facilitating the RecA2 domain to release its grip on DNA and slide in the direction of the RecA1 domain. This

https://doi.org/10.1021/cbmi.4c00077
Chem. Biomed. Imaging 2025, 3, 111−122

systematic tightening and releasing of the RecA-like domains during ssDNA translocation is substantiated by hydrogen/deuterium exchange experiments conducted on SARS-CoV nsp13.[14] As the helicase core RecA1/RecA2 proceeds, the 1B domain retains its position with ssDNA at the initial location and hence is momentarily left in the wake of the helicase core. Given that the 1B domain is tethered to the helicase body via a lengthy stalk domain, this flexible architecture allows for a degree of separation between the 1B and RecA1 domain. When this distance extends (to a maximum of ∼4 bp), tension accumulates to a level that temporarily halts the unwinding process. At this juncture, the 1B domain loosens its grip on DNA, leading to a tension release. Finally, the 1B domain gravitates toward the RecA1 domain, and the initial substrate loading conformation is restored. Our model aligns broadly with the inchworm mechanism described for SF1 helicases. The discrete steps or lags observed in nsp13-catalyzed unwinding are most likely attributed to the 1B and stalk domains, which impart a high degree of flexibility to nsp13 during the unwinding reaction.

METHOD DETAILS

Preparation of Partial Duplex Oligonucleotides

Partial duplex DNA was annealed from an 18/24-bp single-stranded DNA and a 39/45-nt single-stranded DNA. All ssDNA were purchased from Integrated DNA Technologies.

Top Strand 1:5′-CGA AGC TGC TAA CAT CAG-3′-Cy5

Bottom Strand 1:5′-Biotin-TTTTTTTTTTTTTTT-TTTTTTT-Cy3-CTG ATG TTA GCA GCT TCG-3′

Top Strand 2:5′-CGA AGC TGC ATT GTA GTC-3′ -Cy5

Top Strand 3:5′-CGA CAG CGA AGC TGC TAA CAT CAG-3′-Cy5

Bottom Strand 3:5′- Biotin-TTTTTTTTTTTTTTT-TTTTTTT-Cy3-CTG ATG TTA GCA GCT TCG CTG TCG-3′

Top Strand 4:3′-CGA AGC TGC TAA CAT CAG-5′-Cy5

Bottom Strand 4: Cy3−3′-TTTTTTTTTTTTTTT-TTTTTT CTG ATG TTA GCA GCT TCG-Biotin-5′

The Top Strand 1 and Bottom Strand 1 were used to form the partial duplex DNA substrate used in the manuscript and the Supporting Information (Figure S2). Top Strand 1, Bottom Strand 1, and Top Strand 2 were used to form a partial duplex DNA to calibrate the FRET efficiency and unwind the partial duplex DNA length relationship (Figure S5). Top Strand 3 and Bottom Strand 3 were used to form the partial duplex DNA substrate used in the Supporting Information (Figure S6). Top Strand 4 and Bottom Strand 4 were used to form a partial duplex DNA to test the patrolling behavior of the nsp13 (Figure S9).

Subsequently, 4 μL (for Top Strand 2) or 1 μL (for Top Strands 1, 3, and 4) of 100 μM Top Strand and 1 μL of 400 μM Bottom Strand were added to 48 μL of annealing buffer containing 20 mM Tris:HCl (pH 7.5), 50 mM sodium chloride (NaCl), and 0.2 mM ethylenediaminetetraacetic acid (EDTA); the mixture was then incubated at 80 °C for 15 min, followed by slowly cooling it to room temperature. The annealed DNA was diluted to the desired concentrations with T50 buffer (10 mM tris base and 50 mM NaCl, pH 8.0) before use.

Production of MERS-CoV nsp13 and SARS-CoV-2 nsp13

Expression and purification of SARS-CoV nsp13 follows the similar protocol for preparing MERS-CoV nsp13.[11] Briefly, the gene encoding SARS-CoV-2 nsp13 (NCBI Reference Sequence: YP_009725308.1, 1−601aa) was synthesized and inserted into a modified pFastBac1 transfer plasmid, which encodes the N-terminal 6xHis-SUMO-tagged full-length nsp13. A PreScission protease site was engineered between the 6xHis-SUMO tag and the N-terminal sequence of nsp13, which was subsequently used for tag removal. SARS-CoV-2 nsp13 was overexpressed in high-Five insect cells. The helicase was initially purified using Ni-NTA resin, and the N-terminal 6xHis-SUMO tag was subsequently cleaved using the PreScission protease. The final purification step of nsp13 was size-exclusion chromatography using a Superdex 200 10/300 GL column (GE healthcare). Plasmid expressing Walker B mutant E375Q of SARS-CoV-2 nsp13 was generated using the site-directed mutagenesis method, and the E375Q mutant was expressed and purified following the same protocols used for preparing wild-type nsp13.

NTPase Assay

A QuantiChrom ATPase/GTPase assay kit (Universal Biologicals) was used to measure the NTPase activity of the nsp13 helicases. The assays were conducted by following the standard protocol suggested by the manufacturer. Briefly, 20 μL of reaction mixtures contained reaction buffer, 0.05 μM helicase, and 0.125 mM nucleotide triphosphate substrate. The mixtures were incubated at 25 °C, and at time points 0, 1, 2, 3, 4, 5, and 6 min, 100 μL of reagent containing chemicals to stop and generate color for free phosphate (a product of NTPase hydrolysis) was added to the reaction. After incubation at room temperature for 30 min, the OD_{620} of each sample were measured using a SpectraMax M5 plate reader. Using the phosphate standard curve, the concentrations of free phosphate in each reaction were calculated. The enzyme activity of each reaction was calculated as follows:

$$\text{Enzyme Activity} = \frac{[Pi]\ (\mu\text{M}) \times 20\ \mu\text{L}}{5\ \mu\text{L} \times t}\left(\frac{U}{L}\right)$$

1 unit of activity is the amount of enzyme that catalyzes the production of 1 μmol of free phosphate per minute under the assay conditions. t is the reaction time in seconds; enzyme concentration was 0.05 μM.

For each turnover rate assessment, at least six independent measurements were performed to calculate the NTPase hydrolysis rate.

Electrophoretic Mobility Shift Assay (EMSA)

In the reaction mixture (20 μL), purified proteins (MERS-CoV nsp13) were incubated with 50 nM partial duplex DNA (prepared by mixing a top strand 5′-TTT TTT TTT TTT TTT TTT TTT CTG ATG TTA GCA GCT TCG-3′ with a bottom strand 5′-Cy5.5- CGA AGC TGC TAA CAT CAG-3′) in the binding buffer containing 10 mM Tris-HCl, pH8.8, 100 mM NaCl, 4 mM $MgCl_2$, 0.1 mM ATP-γS, 0.5 mM TCEP and 5% glycerol for 30 min at room temperature. After the incubation, the gel was loaded onto the 7.5% Native poly acrylamide gel in 0.5× TG buffer (12.5 mM Tris-HCl, 9.5 mM Glycine, pH 8.8) at 100 V for 100 min on ice. Samples were resolved in the gel and scanned with ChemiDocMP Imagine System (Bio-RAD).

https://doi.org/10.1021/cbmi.4c00077
Chem. Biomed. Imaging 2025, 3, 111−122

Single-Molecule FRET Measurements of DNA Unwinding by Helicase

Preparation of Biotinylated and Poly(ethylene glycol) (PEG) Passivated Quartz Slides and Coverslips.

The quartz slides (with drilled holes 1 in. x 3 in., 1 mm thick, Finkenbeiner, Inc., USA) and the coverslips (24 mm × 40 mm, Corning, USA) were coated with biotin-polyethylene glycol (biotin-PEG) and PEG in order to eliminate nonspecific binding, as well as to generate biotin-NeutrAvidin bridges on the surface. The biotin-PEG and mPEG-succinimidyl valerate were covalently immobilized onto the slide surface according to the established protocol. First, the slides were thoroughly cleaned with household detergent and Milli-Q water, and then they were sonicated in Milli-Q water, acetone (Fisher Scientific, USA), 1 M potassium hydroxide (Fisher Scientific, USA), and methanol (99.8%, Fisher Scientific, USA) for 1 h each. Upon each sonication, the slides were thoroughly washed with Milli-Q water. After that, each quartz slide was burnt with a propane torch for 2 min and immersed in Milli-Q water immediately. The slides were subsequently incubated in methanol containing 1% (v/v) 3-Aminopropyltriethoxysilane (APTES, Sigma, USA) and 5% (v/v) acetone for 10 min, and then, they were incubated for another 10 min after 1 min of sonication. Upon incubation, the slides were thoroughly washed with Milli-Q water and methanol and blow-dried with air. After that, 80 μL mixture of 200 mg/mL methoxy-polyethylene glycol succinimidyl valerate and 36.67 mg/mL biotin-polyethylene glycol succinimidyl valerate (m-PEG-SVA, biotin-PEG-SVA, Laysan Bio Inc., USA) were dropped onto the treated quartz slides, and the cover slides were placed on top of the quartz slides to form a chamber. The chamber was then incubated in a wetbox in the dark overnight at room temperature. Upon incubation, the chamber was carefully separated, and the surfaces were washed thoroughly with Milli-Q water and blow-dried with air. The PEGylation process was repeated. The flow chamber was assembled from a biotin-PEG-coated quartz slide and a coverslip using double-sided tape and epoxy glue.

Immobilization of DNA and Helicase onto the Substrate

The partial-duplex DNA was immobilized onto the substrate by the biotin-NeutrAvidin bridge, and the helicase was specifically bound to the junction of the ssDNA and dsDNA at the partial-duplex DNA. First, 50 μL of 0.1 mg/mL NeutrAvidin (Fisher Scientific, USA) was added into the channels and incubated for 5 min at room temperature. Upon incubation, the unbound NeutrAvidin was washed out with 200 μL of T50 buffer at least three times for each channel. Subsequently, 50 μL of 15 pM partial-duplex DNA was added to the channel and the mixture incubated for 10 min at room temperature. Then, any unbound DNA was washed out with 200 μL of T50 buffer at least three times. After that, 50 μL of 20 nM helicase was injected into the channel and incubated for another 10 min at room temperature. Upon incubation, 50 μL of NTPs at different concentrations in oxygen scavenger solution (0.1 mg/mL glucose oxidase, Sigma, USA; 0.02 mg/mL catalase, Sigma, USA; 0.8% [w/w] dextrose, Sigma, USA; 3 mM 6-hydroxy-2,5,7,8-tetramethylchroman-2-carboxylic acid, Trolox, Sigma, USA in T50 buffer) was injected into the channel. The volume of NTPs was five times larger than the channel volume; thus, it could flush out any unbound helicases from the channel. The sample was imaged immediately after NTPs injection.

Single-Molecule Imaging Through Total Internal Reflection Fluorescence Microscopy (TIRF)

The DNA unwinding events by the helicase were recorded with a homemade TIRF microscope. The detailed structure of the microscope was previously reported. Specifically, the Cy5-labeled sample was excited by a 633 nm laser beam, while the Cy3-labeled sample was excited by a 532 nm laser beam, which was also used for FRET measurements. Videos were taken with a 100 ms exposure time, and 600 frames were recorded. Obtained data were analyzed in real time using custom software obtained from Dr. Taekjip Ha's group at Harvard Medical School.

■ ASSOCIATED CONTENT

Supporting Information

The Supporting Information is available free of charge at https://pubs.acs.org/doi/10.1021/cbmi.4c00077.

Additional experimental smFRET traces, plots, analysis, gel images, unwinding data, protein purification results, and associated data points (PDF)

■ AUTHOR INFORMATION

Corresponding Authors

Hamza Balci − *Department of Physics, Kent State University, Kent, Ohio 44242, United States;* orcid.org/0000-0002-0273-4871; Email: hbalci@kent.edu

Sheng Cui − *NHC Key Laboratory of Systems Biology of Pathogens, National Institute of Pathogen Biology, Chinese Academy of Medical Sciences and Peking Union Medical College, Beijing 100730, China;* orcid.org/0000-0001-6329-3582; Email: cui.sheng@ipb.pumc.edu.cn

Jiajie Diao − *Department of Cancer Biology, University of Cincinnati College of Medicine, Cincinnati, Ohio 45267, United States;* orcid.org/0000-0003-4288-3203; Email: jiajie.diao@uc.edu

Authors

Wei Hao − *NHC Key Laboratory of Systems Biology of Pathogens, National Institute of Pathogen Biology, Chinese Academy of Medical Sciences and Peking Union Medical College, Beijing 100730, China*

Xiao Hu − *Department of Cancer Biology, University of Cincinnati College of Medicine, Cincinnati, Ohio 45267, United States*

Qixin Chen − *Department of Cancer Biology, University of Cincinnati College of Medicine, Cincinnati, Ohio 45267, United States*

Bo Qin − *NHC Key Laboratory of Systems Biology of Pathogens, National Institute of Pathogen Biology, Chinese Academy of Medical Sciences and Peking Union Medical College, Beijing 100730, China*

Zhiqi Tian − *Department of Cancer Biology, University of Cincinnati College of Medicine, Cincinnati, Ohio 45267, United States*

Ziheng Li − *NHC Key Laboratory of Systems Biology of Pathogens, National Institute of Pathogen Biology, Chinese Academy of Medical Sciences and Peking Union Medical College, Beijing 100730, China*

Pengjiao Hou − *NHC Key Laboratory of Systems Biology of Pathogens, National Institute of Pathogen Biology, Chinese*

Academy of Medical Sciences and Peking Union Medical College, Beijing 100730, China

Rong Zhao − *NHC Key Laboratory of Systems Biology of Pathogens, National Institute of Pathogen Biology, Chinese Academy of Medical Sciences and Peking Union Medical College, Beijing 100730, China*

Complete contact information is available at: https://pubs.acs.org/10.1021/cbmi.4c00077

Author Contributions

#W.H. and X.H. contributed equally. S.C. and J.D. designed and directed the study. X.H. performed single-molecule measurements and analyzed data. W.H., B.Q., Z.L., P.H., and R.Z. purified proteins and conducted bulk experiments. All authors discussed the results and wrote the manuscript.

Notes

The authors declare no competing financial interest.

■ ACKNOWLEDGMENTS

S.C. was supported by CRP-ICGEB Research Grant 2019 (Grant number: CRP/CHN19-02) and National Key Research and Development Program of China (Grant number: 2016YFD0500300). J.D. was supported by the Special Coronavirus (COVID-19) Research Pilot Grant Program from University of Cincinnati College of Medicine. We thank Drs. Gwangrog Lee and Ruobo Zhou for fruitful discussion.

■ REFERENCES

(1) Drosten, C.; Gunther, S.; Preiser, W.; van der Werf, S.; Brodt, H. R.; Becker, S.; Rabenau, H.; Panning, M.; Kolesnikova, L.; Fouchier, R. A.; et al. Identification of a novel coronavirus in patients with severe acute respiratory syndrome. *New England journal of medicine* **2003**, *348*, 1967−1976.

(2) Ksiazek, T. G.; Erdman, D.; Goldsmith, C. S.; Zaki, S. R.; Peret, T.; Emery, S.; Tong, S.; Urbani, C.; Comer, J. A.; Lim, W.; et al. A novel coronavirus associated with severe acute respiratory syndrome. *New England journal of medicine* **2003**, *348*, 1953−1966.

(3) Zaki, A. M.; van Boheemen, S.; Bestebroer, T. M.; Osterhaus, A. D.; Fouchier, R. A. Isolation of a novel coronavirus from a man with pneumonia in Saudi Arabia. *New England journal of medicine* **2012**, *367*, 1814−1820.

(4) Coronaviridae Study Group of the International Committee on Taxonomy of, V. The species Severe acute respiratory syndrome-related coronavirus: classifying 2019-nCoV and naming it SARS-CoV-2. *Nature microbiology* **2020**, *5*, 536−544.

(5) Zhu, N.; Zhang, D.; Wang, W.; Li, X.; Yang, B.; Song, J.; Zhao, X.; Huang, B.; Shi, W.; Lu, R.; et al. A Novel Coronavirus from Patients with Pneumonia in China, 2019. *New England journal of medicine* **2020**, *382*, 727−733.

(6) Chan, J. F.; Yuan, S.; Kok, K. H.; To, K. K.; Chu, H.; Yang, J.; Xing, F.; Liu, J.; Yip, C. C.; Poon, R. W.; et al. A familial cluster of pneumonia associated with the 2019 novel coronavirus indicating person-to-person transmission: a study of a family cluster. *Lancet* **2020**, *395*, 514−523.

(7) Newman, J. A.; Douangamath, A.; Yadzani, S.; Yosaatmadja, Y.; Aimon, A.; Brandão-Neto, J.; Dunnett, L.; Gorrie-Stone, T.; Skyner, R.; Fearon, D.; et al. Structure, mechanism and crystallographic fragment screening of the SARS-CoV-2 NSP13 helicase. *Nat. Commun.* **2021**, *12*, 4848.

(8) Ivanov, K. A.; Thiel, V.; Dobbe, J. C.; van der Meer, Y.; Snijder, E. J.; Ziebuhr, J. Multiple enzymatic activities associated with severe acute respiratory syndrome coronavirus helicase. *Journal of virology* **2004**, *78*, 5619−5632.

(9) Adedeji, A. O.; Lazarus, H. Biochemical Characterization of Middle East Respiratory Syndrome Coronavirus Helicase. *mSphere* **2016**, DOI: 10.1128/mSphere.00235-16.

(10) Hao, W.; Wojdyla, J. A.; Zhao, R.; Han, R.; Das, R.; Zlatev, I.; Manoharan, M.; Wang, M.; Cui, S. Crystal structure of Middle East respiratory syndrome coronavirus helicase. *PLoS Pathog* **2017**, *13*, e1006474.

(11) Cui, S.; Hao, W. Deducing the Crystal Structure of MERS-CoV Helicase. *Methods in molecular biology* **2020**, *2099*, 69−85.

(12) Sommers, J. A.; Loftus, L. N.; Jones, M. P., 3rd; Lee, R. A.; Haren, C. E.; Dumm, A. J.; Brosh, R. M., Jr. Biochemical analysis of SARS-CoV-2 Nsp13 helicase implicated in COVID-19 and factors that regulate its catalytic functions. *J. Biol. Chem.* **2023**, *299*, 102980.

(13) Lee, N. R.; Kwon, H. M.; Park, K.; Oh, S.; Jeong, Y. J.; Kim, D. E. Cooperative translocation enhances the unwinding of duplex DNA by SARS coronavirus helicase nsP13. *Nucleic acids research* **2010**, *38*, 7626−7636.

(14) Jia, Z.; Yan, L.; Ren, Z.; Wu, L.; Wang, J.; Guo, J.; Zheng, L.; Ming, Z.; Zhang, L.; Lou, Z.; Rao, Z. Delicate structural coordination of the Severe Acute Respiratory Syndrome coronavirus Nsp13 upon ATP hydrolysis. *Nucleic Acids Res.* **2019**, *47*, 6538−6550.

(15) Saikrishnan, K.; Powell, B.; Cook, N. J.; Webb, M. R.; Wigley, D. B. Mechanistic basis of 5′-3′ translocation in SF1B helicases. *Cell* **2009**, *137*, 849−859.

(16) Adedeji, A. O.; Marchand, B.; Te Velthuis, A. J.; Snijder, E. J.; Weiss, S.; Eoff, R. L.; Singh, K.; Sarafianos, S. G. Mechanism of nucleic acid unwinding by SARS-CoV helicase. *PloS one* **2012**, *7*, e36521.

(17) Yu, J.; Im, H.; Lee, G. Unwinding mechanism of SARS-CoV helicase (nsp13) in the presence of Ca(2+), elucidated by biochemical and single-molecular studies. *Biochem. Biophys. Res. Commun.* **2023**, *668*, 35−41.

(18) Belon, C. A.; Frick, D. N. Fuel Specificity of the Hepatitis C Virus NS3 Helicase. *J. Mol. Biol.* **2009**, *388*, 851−864.

(19) Mickolajczyk, K. J.; Shelton, P. M. M.; Grasso, M.; Cao, X.; Warrington, S. E.; Aher, A.; Liu, S.; Kapoor, T. M. Force-dependent stimulation of RNA unwinding by SARS-CoV-2 nsp13 helicase. *Biophysical journal* **2021**, *120*, 1020.

(20) Kim, J. L.; Morgenstern, K. A.; Griffith, J. P.; Dwyer, M. D.; Thomson, J. A.; Murcko, M. A.; Lin, C.; Caron, P. R. Hepatitis C virus NS3 RNA helicase domain with a bound oligonucleotide: the crystal structure provides insights into the mode of unwinding. *Structure* **1998**, *6*, 89−100.

(21) Velankar, S. S.; Soultanas, P.; Dillingham, M. S.; Subramanya, H. S.; Wigley, D. B. Crystal structures of complexes of PcrA DNA helicase with a DNA substrate indicate an inchworm mechanism. *Cell* **1999**, *97*, 75−84.

(22) Dillingham, M. S.; Soultanas, P.; Wiley, P.; Webb, M. R.; Wigley, D. B. Defining the roles of individual residues in the single-stranded DNA binding site of PcrA helicase. *Proc. Natl. Acad. Sci. U.S.A.* **2001**, *98*, 8381−8387.

(23) Singleton, M. R.; Scaife, S.; Wigley, D. B. Structural analysis of DNA replication fork reversal by RecG. *Cell* **2001**, *107*, 79−89.

(24) Buttner, K.; Nehring, S.; Hopfner, K. P. Structural basis for DNA duplex separation by a superfamily-2 helicase. *Nature structural & molecular biology* **2007**, *14*, 647−652.

(25) Betterton, M. D.; Julicher, F. Opening of nucleic-acid double strands by helicases: active versus passive opening. *Physical review. E, Statistical, nonlinear, and soft matter physics* **2005**, *71*, 011904.

(26) Manosas, M.; Xi, X. G.; Bensimon, D.; Croquette, V. Active and passive mechanisms of helicases. *Nucleic acids research* **2010**, *38*, 5518−5526.

(27) Myong, S.; Bruno, M. M.; Pyle, A. M.; Ha, T. Spring-loaded mechanism of DNA unwinding by hepatitis C virus NS3 helicase. *Science* **2007**, *317*, 513−516.

(28) Cheng, W.; Arunajadai, S. G.; Moffitt, J. R.; Tinoco, I., Jr.; Bustamante, C. Single-base pair unwinding and asynchronous RNA release by the hepatitis C virus NS3 helicase. *Science* **2011**, *333*, 1746−1749.

(29) Manosas, M.; Spiering, M. M.; Ding, F.; Croquette, V.; Benkovic, S. J. Collaborative coupling between polymerase and helicase for leading-strand synthesis. *Nucleic acids research* **2012**, *40*, 6187−6198.
(30) Ribeck, N.; Kaplan, D. L.; Bruck, I.; Saleh, O. A. DnaB helicase activity is modulated by DNA geometry and force. *Biophysical journal* **2010**, *99*, 2170−2179.
(31) Johnson, D. S.; Bai, L.; Smith, B. Y.; Patel, S. S.; Wang, M. D. Single-molecule studies reveal dynamics of DNA unwinding by the ring-shaped T7 helicase. *Cell* **2007**, *129*, 1299−1309.
(32) Yue, K.; Yao, B.; Shi, Y.; Yang, Y.; Qian, Z.; Ci, Y.; Shi, L. The stalk domain of SARS-CoV-2 NSP13 is essential for its helicase activity. *Biochem. Biophys. Res. Commun.* **2022**, *601*, 129−136.

https://doi.org/10.1021/cbmi.4c00077
Chem. Biomed. Imaging 2025, 3, 111−122